Supporting Information

Tubulin bond energies and microtubule biomechanics determined from nanoindentation *in silico*

Olga Kononova,[a,b] Yaroslav Kholodov,[b] Kelly E. Theisen,[c] Kenneth A. Marx[a], Ruxandra I. Dima,[c] Fazly I. Ataullakhanov[d,e,], Ekaterina L. Grishchuk[f,*], and Valeri Barsegov[a,b,*]

[a]Department of Chemistry, University of Massachusetts, Lowell, MA 01854, USA; [b]Moscow Institute of Physics and Technology, Moscow region, 141700, Russia; [c]Department of Chemistry, University of Cincinnati, Cincinnati, OH 45221, USA; [d]Center for Theoretical Problems of Physicochemical Pharmacology, Russian Academy of Sciences, Moscow 119991, Russia; [e]Physics Department, Moscow State University, Moscow 119991, Russia; [f]Physiology Department, Perelman School of Medicine, University of Pennsylvania, Philadelphia, PA 19104

Supporting Materials and Methods

Constructing the ring structure of αβ-tubulin dimers: As a starting point for our computer model of a fragment of a MT cylinder we used the model from the published work of Wells and Aksimentiev.[1] To build the model, Wells and Aksimentiev used the all-atom Molecular Dynamics Flexible Fitting (MDFF) method to generate an atomistic structure for an MT lattice starting from the cryo-EM map of the lattice[2] and the atomistic structure of the tubulin subunit from X-ray crystallography (PDB entry: 1JFF).[3] The MDFF method locates tubulin subunits in the cryo-EM map by testing all plausible subunit locations by re-adjusting position of the atomic tubulin structure to achieve maximum correspondence to the cryo-EM data. Only standard potential energy functions (atomic force fields) implemented in all-atom Molecular Dynamics (MD) simulations were used without any simplifying assumptions about the shapes of these bond energies and without using the attractive potentials. Using this approach, two fragments were created: two protofilaments connected by lateral contacts as in the bulk of 13_3 MT lattice (system N), and two protofilaments connected by lateral contacts as seen at the seam in 13_3 structure (system S). By lateral contacts we mean a set of binary contacts between the amino acid residues forming the interfaces between adjacent tubulin monomers in neighboring protofilaments, as identified by the above MDFF procedure. Specifically, coordinates for one protofilament were obtained by Wells and Aksimentiev using rigid-fitting of the tubulin dimer into a subset of the cryo-EM map (CoLoRes program), and the best fit was saved. Coordinates for a second protofilament were obtained from the first protofilament by a rotation of 360^o /13 about the map's center, and an axial protofilament displacement of 3/2 dimer subunit. Then, the full cylindrical structure was built by assembling 12 copies of the N-type PFs and one copy of the S-type protofilament into 360^o/13 radial sectors. Next, the all-atom Molecular Dynamics simulations in explicit solvent (i.e. fully water-solvated protein system plus ions to neutralize charges on polypeptide chains) were used by Wells and Aksimentiev to determine the best possible configuration of all subunits in this system. This configuration corresponded to the minimum of the total (kinetic plus potential) energy of the system. No other kinetic or thermodynamic information has been used during the energy minimization step. All system elements were allowed to change their conformation to make the system capable of reaching the state of equilibrium with energy minimum. A similar approach has been used extensively to determine atomistic structures for large biomolecular complexes, including HIV-1 capsid structure,[4] the ribosome-SecYE complex,[5] the monomeric yeast and mammalian Sec61 complexes interacting with the translating ribosome,[6] the Trypanosoma brucei ribosome,[7] the yeast 26S proteasome,[8] and the no-go mRNA decay complex Dom34-Hbs1 bound to a stalled 80S ribosome.[9]

Data analyses:

1) *Structure visualization* was performed using the VMD package.[10] To quantify the extent of structural

similarity between a given conformation and a native (reference) state, we used the structure overlap function, $\chi(t) = (2N(N-1))^{-1}\sum\Theta(|r_{ij}(t) - r_{ij}^0| - \beta r_{ij}^0)$, where in the Heaviside step function $r_{ij}(t)$ and r_{ij}^0 are the inter-particle distances between the *i*-th and *j*-th residues in the transient structure and in the native state, respectively, and β = 0.2 is the tolerance for the inter-particle distance change.

2) *Mechanical deformation of MT cylinder*: We used the thin shell approximation[11,12] to analyze the flexural rigidity of the MT cylinder, according to which the slope of the *FX* curve for small *X* is given by $K_{MT} = 1.18Et^{5/2}/R^{3/2}$, where t = 1.1 nm is the cylinder thickness, R = 12.5 nm is the exterior radius, and E is the Young's modulus. We assume that the MT cylinder is roughly isotropic prior to disruption of lateral contacts. The bending rigidity of the MT cylinder was estimated as the product $EI = E \times I$, where I is the moment of inertia of the MT cylinder with respect to the longitudinal axis. Since the MT cylinder is composed of n = 13 identical protofilaments of radius r = 2.5 nm, the moment of inertia can be calculated as $I = (2/\pi^2 n^3 + n)\pi/4r^4$. The persistence length was estimated by using the formula $L_p = EI/k_BT$.

3) *Bending deformation of protofilament fragments:* By performing numerical integration, the force-deformation (*F* vs. *X*) profiles obtained from bending simulations were transformed into the profiles of bending energy $V = \int F(X)dX$ vs. *X* (*the inset* in Fig. S5). To estimate the flexural rigidity for each protofilament, we calculated the energy of bending of the beam, $V = \frac{EI}{2}\int_L (1/R - 1/R_0)^2 dl$, where R_0 and R are the radii of the curvature of the protofilament in the initial state, used as a reference structure, and the final state, respectively; *dl* is the length element; and L is the total length.[11] This is a harmonic approximation valid only for small deformations *X*. To find the range of *X* for which this approximation is valid, we performed a fit of the quadratic function $V \sim X^2$ to the curves of the bending energy (dashed black line in *the inset* in Fig. S5). In the initial state, the protofilament is straight, and, hence, $1/R_0 = 0$. To simplify calculations, we only considered the protofilament portion of constant curvature, in which case $V = EIL/(2R^2)$. Knowing V and R allows us to calculate $EI = 2VR^2/L$. Using the simulation output, we estimated R using the formula for the radius of the arc $R = X/2 + C^2/(8X)$, where C is the end-to-end distance (Fig. S5). The persistence length for each protofilament fragments was calculated using the formula: $L_p = EI/k_BT$.

4) *Estimation of ΔG_{lat} and ΔG_{long}:* We analyzed the energy output from simulations (potential energy U_{SOP}) to estimate the enthalpy change of deformation ΔH. The total work of deformation w can be obtained by integrating the area under the *FX* curve for the forward indentation. This procedure can then be repeated for the retraction curve to resolve the reversible part of work $w_{rev} = \Delta G = \Delta H - T\Delta S$ and the entropic contribution $T\Delta S = \Delta H - w_{rev}$. We used this approach to resolve the free energy change associated with the rupture of lateral and

longitudinal bonds. First, we carefully selected two short time intervals within the same trajectory, one showing the dissociation of lateral interfaces and the other showing the dissociation of longitudinal interfaces. Next, for each selected portion of the trajectory we calculated the number of dissociated lateral interfaces n_{lat} and longitudinal interfaces n_{long}, and estimated the total reversible work w_{lat} and w_{long}. The quantities w_{lat} and w_{long} were calculated by integrating the corresponding regions in the *FX* curve for the forward indentation and the backward retraction. The amount of dissipated energy (irreversible part of work w_{irrev}) was estimated using the Crooks theorem (see next paragraph). The free energy of dissociation per single lateral (longitudinal) bond was calculated by taking the ratio $\Delta G_{lat} = w_{lat}/ n_{lat}$ ($\Delta G_{long} = w_{long}/ n_{long}$).

5) *Calculation of reversible work w_{rev}:* Crooks showed theoretically[13] and the Bustamante lab verified experimentally (using single-molecule measurements on an RNA molecule[14]) that in a driven unfolding process from the initial point $X = X_{in}$ to some final point $X = X_{fin}$ and a reverse refolding process from $X = X_{fin}$ back to $X = X_{in}$, the probability distributions (histograms) of the values of work for the forward process $p_{unf}(w)$ and reverse process $p_{ref}(-w)$ are connected via the relationship:

$$p_{unf}(w) \Big/ p_{ref}(-w) = \exp\left[-\left(w - \Delta G_{eq}\right) \Big/ k_B T \right]$$

The point at which $p_{unf}(w)$ and $p_{ref}(-w)$ intersect corresponds to the equilibrium work $w = \Delta G_{eq}$. In our simulations, we are limited to 3 trajectories for each indentation point 1-7 (Fig. 1C). We can still use the Crooks relationship if we notice that $p_{unf}(w)$ and $p_{ref}(-w)$ intersect at their tails, which correspond to the extreme observations: the minimum work ($w_{min,forw}$) for the forward process and the maximum work ($w_{max,rev}$) for the reverse process ($w_{max,ref} < w_{min,forw}$). Hence, the reversible work is between the minimum work for the forward process and the maximum work for the reverse process, i.e. $w_{max,rev} < w < w_{min.forw}$. In the context of our indentation experiments *in silico*, this corresponds to the minimum work $w_{min,ind} = min\{w_{1,ind}, w_{2,ind,} \ldots\}$ for the forward forced indentation process ($p_{ind}(w)$) and the maximum work $w_{max,ret} = max\{w_{1,ret}, w_{2,ret,} \ldots\}$ for the backward force-quenched retraction process ($p_{ret}(w)$)), i.e. $w_{max,ret} < w < w_{min,ind}$. We estimated reversible work $w_{rev} = \Delta G_{eq}$ by taking the arithmetic mean of $w_{max,ret}$ and $w_{min,ind}$, i.e. . $w \approx (w_{min,ind} + w_{max,ret})/2$.

6) *Estimation of the range of lateral and longitudinal bonds:* We examined the forced-induced flattening of the ring of tubulin dimers under the tip in the lateral direction ΔY_{lat} and elongation of MT protofilaments in the longitudinal direction ΔY_{long} (Fig. S3). We related the indentation depth X to the resulting changes in MT-tip contact area along the cylinder axis and in the transverse direction. Corresponding to $X \approx$ 6-8 nm indentation, when the lateral contacts become disrupted (force plateau in *FX* curves and structure 2a in Fig. 4), the elongation of the tubulin ring is $\Delta Y_{lat} \approx$ 3.3 nm. From structure analysis we found the number of lateral interfaces under the tip to be N_{lat} = 3-4 (Fig. S3B, S3C). These were used to estimate the average extension per

lateral interface at which the dissociation occurs, $\Delta y_{lat} = \Delta Y_{lat}/N_{lat} \approx 0.85$-1.1 nm. Next, the longitudinal contacts become disrupted at $X \approx$ 9-11 nm indentation (force peak in the *FX* curves and structure 2b in Fig. 4), for which the elongation of 3-4 dimer-long portion of an MT protofilament under the tip is $\Delta Y_{long} \approx 7.5$ nm. Analysis of structures showed that the number of longitudinal interfaces involved was $N_{long} \approx$ 5-6 (Fig. S3B, S3C) Hence, the average extension for dissociation of the longitudinal interface is $\Delta y_{long} = \Delta Y_{long}/N_{long} \approx 1.25$-1.5 nm.

Supporting References:

1. Wells, D.B., Aksimentiev, A. *Biophys. J.* **2010,** *99*, 629–637.
2. Li, H., DeRosier, D.J., Downing, K.H. *Structure*. **2002,** *10*, 1317-1328.
3. Lowe, J., Li, H., Downing, K.H., Nogales, E. *J. Mol. Biol.* **2001,** *313*, 1045–1057.
4. Zhao, G., Perilla, J.R., Yufenyuy, E.L., Meng, X., Chen, B., Ning, J., Ahn, J., Gronenborn, A.M., Schulten, K., Aiken, C., Zhang, P. *Nature* **2013,** *497*, 643-646.
5. Frauenfeld, J., Gumbart, J., van der Sluis, E.O., Funes, S., Gartmann, M., Beatrix, B., Mielke, T., Berninghausen, O., Becker, T., Schulten, K., Beckmann, R. *Nat. Struct. Mol. Biol.* **2011,** *18*, 614-621.
6. Becker, T., Mandon, E., Bhushan, S., Jarasch, A., Armache, J.-P., Funes, S., Jossinet, F., Gumbart, J., Mielke, T., Berninghausen, O., Schulten, K., Westhof, E., Gilmore, R., Beckmann, R. *Science* **2009,** *326*, 1369-1373.
7. Hashem, Y., des Georges, A., Fu, J., Buss, S.N., Jossinet, F., Jobe, A., Zhang, Q., Liao, H.Y., Grassucci, R.A., Bajaj, C., Westhof, E., Madison-Antenucci, S., Frank, J. *Nature* **2013,** *494*, 385-389.
8. Beck, F., Unverdorben, P., Bohn, S., Schweitzer, A., Pfeifer, G., Sakata, E., Nickell, S., Plitzko, J.M., Villa, E., Baumeister, W., Förster, F. *Proc. Natl. Acad. Sci. USA* **2012,** *109*, 14870-14875.
9. Becker, T., Armache, J.-P., Jarasch, A., Anger, A.M., Villa, E., Sieber, H., Motaal, B.A., Mielke, T., Berninghausen, O., Beckmann, R. *Nat. Struct. Mol. Biol.* **2011,** 18:715-720.
10. Humphrey, W., Dalke, A., Schulten, K. *J. Mol. Graphics* **1996,** *14*, 33-38.
11. Landau, L.D., Lifshitz, E.M. Theory of Elasticity, *Theoretical Physics*, 3rd Ed., Elsevier, 1986; Vol. 7.
12. de Pablo, P.J., Schaap, I.A.T., MacKintosh, F.C., Schmidt, C.F. *Phys. Rev. Lett*. **2003,** *91*, 098101-098104.
13. Crooks, G. E. *Phys. Rev. E.* **1999**, *60*, 2721-2726.
14. Collin, D., Ritort, F., Jarzynski, C., Smith, S. B., Tinoco, I., Bustamante, C. *Nature*, **2005**, *437*, 231-234.
15. Xiao, H., Verdier-Pinard, P., Fernandez-Fuentes, N., Burd, B., Angeletti, R., Fiser, A., Horwitz, S. B., Orr, G. A. *Proc. Natl. Acad. Sci. USA* **2006**, *103*, 10166-10173.
16. Grafmüller, A., Noya, E. G., Voth, G. A. *J. Mol. Biol.* **2013**, *425*, 2232-2246.

Supporting Tables

Table S1: Summary of microscopic transitions. These transitions accompany the mechanical compression and collapse of the MT lattice probed at seven unique indentation points 1-7 (Fig. 1C in main text).

Indentation point	Summary of transitions
1	bending; disruption of 20 lateral interfaces; disruption of 5 longitudinal interfaces
2	bending; disruption of 24 lateral interfaces; disruption of 3 longitudinal interfaces
3	bending; disruption of 23 lateral interfaces; disruption of 4 longitudinal interfaces
4	bending; disruption of 16 lateral interfaces; disruption of 3 longitudinal interfaces
5	bending; disruption of 18 lateral interfaces; disruption of 3 longitudinal interfaces
6	bending; disruption of 19 lateral interfaces; disruption of 4 longitudinal interfaces
7	bending; disruption of 21 lateral interfaces; disruption of 4 longitudinal interfaces

Table S2: Comparison of the mechanical and thermodynamic parameters from indentations at different points on the MT lattice. Simulations were carried out using v_f = 1.0 μm/s, and R_{tip} = 10 and 15 nm. Presented are the values of critical force F^*, critical indentation depth X^*, and spring constant K_{MT}. Also shown are the enthalpy change ΔH, and free energy change ΔG associated with the dissociation of lateral and longitudinal bonds.

Indentation point	F^*,nN		X^*,nm		K_{MT},pN/nm		ΔG_{lat}, kcal/mol		ΔG_{long}, kcal/mol		ΔH_{lat}, kcal/mol		ΔH_{long}, kcal/mol	
	10nm	15nm	10 nm	15 nm	10 nm	15 nm	10 nm	15nm	10 nm	15 nm	10 nm	15 nm	10 nm	15 nm
1	0.67	0.72	12.5	12.0	51	53	6.5	6.6	15.0	16.1	8.4	10.2	27.1	29.1
2	0.71	0.78	12.3	12.4	48	54	6.7	7.2	13.4	17.0	9.3	10.1	21.8	23.9
3	0.67	0.77	11.9	12.6	48	58	6.4	6.8	13.9	16.9	9.5	9.7	24.3	27.8
4	0.60	0.73	11.3	10.9	55	61	7.1	7.6	12.5	13.6	9.4	9.8	25.0	27.7
5	0.54	0.80	10.5	11.0	53	57	6.6	7.2	12.5	16.7	7.9	8.6	26.1	26.3
6	0.54	0.71	10.3	10.8	54	66	6.3	7.1	17.8	16.2	8.2	8.8	21.7	24.0
7	0.63	0.74	10.8	10.9	55	65	7.1	7.3	14.3	16.2	10.4	10.5	26.7	27.8

Table S3: Parameterization of the SOP model for the MT lattice. Summarized for each group of residue-residue contacts 1-5 are the average number of native contacts (N_{nb}), the average energy of non-covalent (non-bonded) interactions (E_{nb}), and the average strength of non-covalent interactions per contact (ε_h).

Contacts type	N_{nb}	E_{nb}, kcal/mol	ε_h , kcal/mol
intra-monomer contacts (α-tubulin)	1340	2345	1.8
intra-monomer contacts (β-tubulin)	1240	2320	1.9
intra-dimer contacts	78	150	1.9
longitudinal inter-dimer contacts	38	37.6	1.0
lateral inter-dimer contacts	20	17.6	0.9

Table S4: Major structural determinants of the α- and β-tubulin monomers involved in formation of inter-monomer contacts: Analysis of contacts was performed for a 10 ns trajectory of equilibrium dynamics of the MT lattice (fragment MT8/13) in implicit solvent at T = 300 K. A pair of amino acids was assumed to form a binary contact if the distance between their C_α-atoms was shorter than 8 Å. The secondary structure assignment is the same as in Refs. (15,16).

Contacts type	Structure elements
intra-dimer contacts	α-tubulin: loops T3, T5, H6-H7, and H11-H12; helices H2, H6, and H11 β-tubulin: loops H1-S2, T4, T7, S8-H10, and H10-S9; helices H8 and H10; β-strands S1 and S9
longitudinal inter-dimer contacts	α-tubulin: loops T7 and H10-S9; helices H8, H10, and H12; β-strands S1 and S9 β-tubulin: loops S2-H2, T3, T5, and H6-H7; helices H2 and H11; β-strand S3
lateral inter-dimer contacts	1st monomer (α- or β-tubulin): loops H1-S2, and T2; helix H3 2nd monomer (α- or β-tubulin): M-loop; helices H6, H9, and H10

Supporting Movie Legends

Movie S1. Dynamic force spectroscopy *in silico*: Forced indentation of microtubule lattice between protofilaments. The movie shows the forced indentation experiment *in silico* on the MT, in which a compressive force is applied in between the protofilaments at the indentation point 6 (side view). The MT cylinder (MT8/13) is positioned on a solid mica surface (not shown), as in Fig. 1B. The cantilever base (virtual particle) is moving with the velocity v_f = 1.0 μm/s perpendicular to the surface of the MT cylinder (not shown). As a result, the cantilever tip (gray colored sphere of radius R_{tip} = 10 nm) exerts pressure onto the outer surface of the MT, which undergoes a series of transformations: from continuous deformation at the early stage of indentation to the discrete transitions later in the sequence of events. These visible transitions include the dissociation of the lateral bonds between the protofilaments, and then longitudinal bonds between the tubulin dimers. The movie stops when the indentation depth reaches X = 23 nm. The duration of this indentation experiment is ~50 ms and the length of the movie is ~12 s (the movie is played ~240 times slower than experiment).

Movie S2. Dynamic force spectroscopy *in silico*: Forced indentation and force-quenched tip retraction of microtubule lattice between protofilaments. The movie shows initially the forced indentation of the MT (similar to Movie S1: MT8/13; indentation point 6, v_f = 1.0 μm/s, R_{tip} = 10 nm), in which a compressive force is applied in between the protofilaments (side view). After the indentation depth has reached X = 20 nm, the tip motion is reversed and the force is slowly quenched to zero. The movie stops after the cantilever tip reaches the initial point (X = 0 nm indentation). Partial MT cylinder restructuring is observed during the tip retraction, which includes re-formation of the lateral bonds but not longitudinal bonds. The duration of this indentation-retraction experiment is ~70 ms and the length of the movie is ~18 s (movie is played ~257 times slower than experiment).

Movie S3. Dynamic force spectroscopy *in silico*: Force deformation of 16-dimers long microtubule protofilament. The movie shows the forced deformation experiment *in silico*, in which a compressive force is applied to a single MT protofilament (PF16/1) clamped at both ends (side view). As in Movies S1 and S2, the cantilever base (virtual particle) is moving perpendicular to the PF16/1surface with velocity v_f = 0.2 μm/s (not shown). This results in the cantilever tip (gray colored sphere of radius R_{tip} = 10 nm) exerting pressure on the protofilament. The movie shows that the pressure increase leads to the protofilament bending (initially) and to the dissociation of longitudinal bonds (later). The duration of this deformation experiment is ~90 ms and the length of the movie is ~15 s (movie is played ~167 times slower than experiment).

Supporting Figures.

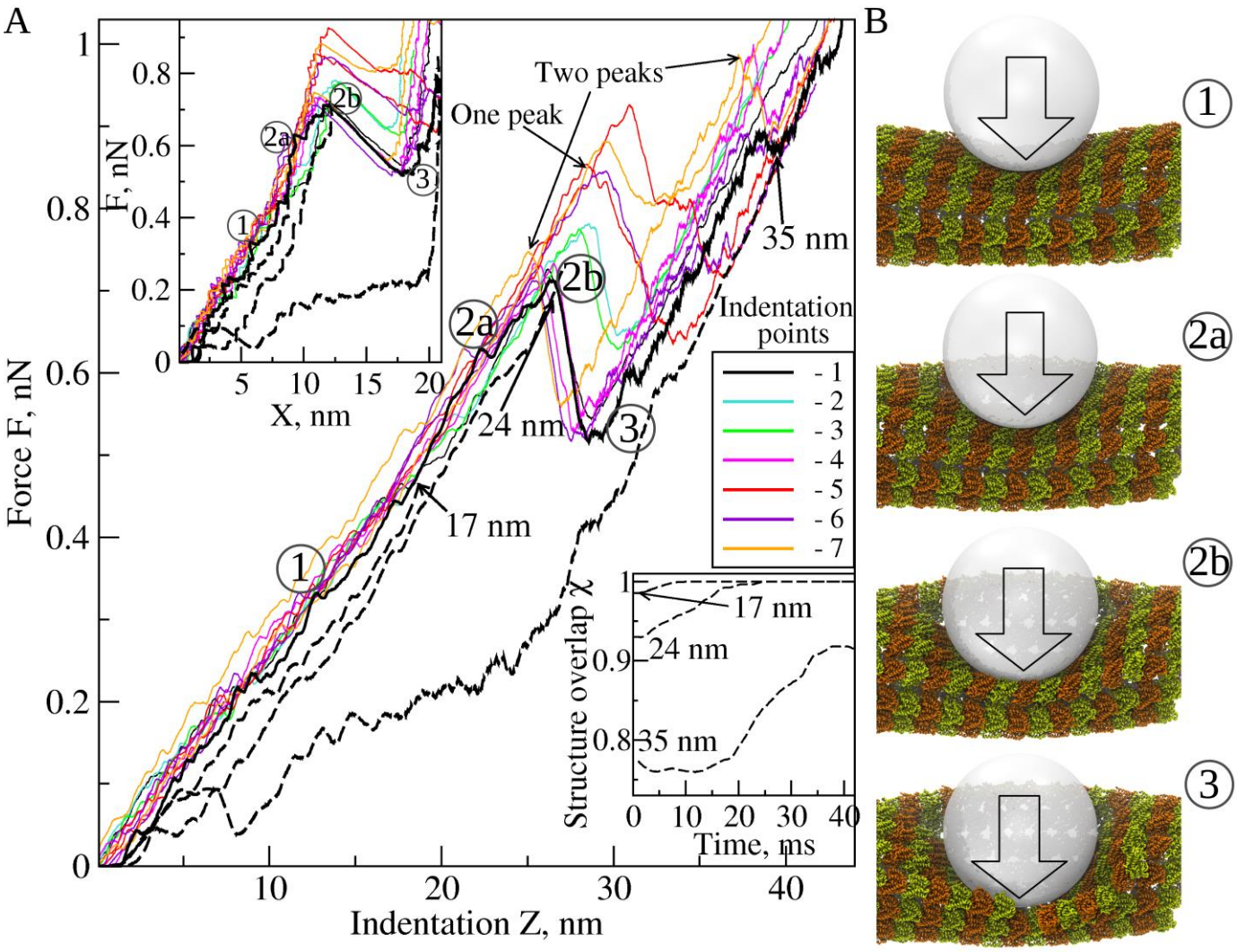

Fig. S1. Forced indentation of MT lattice as in Fig. 2 but for a larger tip. A: The force-deformation (*FZ*) curves for 7 indentation points (Fig. 1C) obtained with v_f =1.0 μm/s and R_{tip} = 15 nm (see Fig. 2 for results obtained with smaller tip of R_{tip} = 10 nm). The curves are shown in different color for clarity. Dashed black curves represent the *FZ* profiles for the tip retraction simulations, which followed the forward indentations (solid black curve) with *Z* = 17, 24, and 35 nm as initial conditions. *The top inset* shows the corresponding *FX* curves for the forward indentation (solid curves; colors as in A) and backward tip retraction (dashed black curves). *The bottom inset* shows the time profiles of the structure overlap χ for MT lattice restructuring during tip retraction (starting from *Z* = 17, 24, and 35 nm indentation). **B:** The MT structures 1, 2a, 2b, and 3, illustrating the mechanism of MT deformation and collapse (as in Fig. 2 in the main text), which correspond to the accordingly numbered regions in the force-deformation curves in **A.**

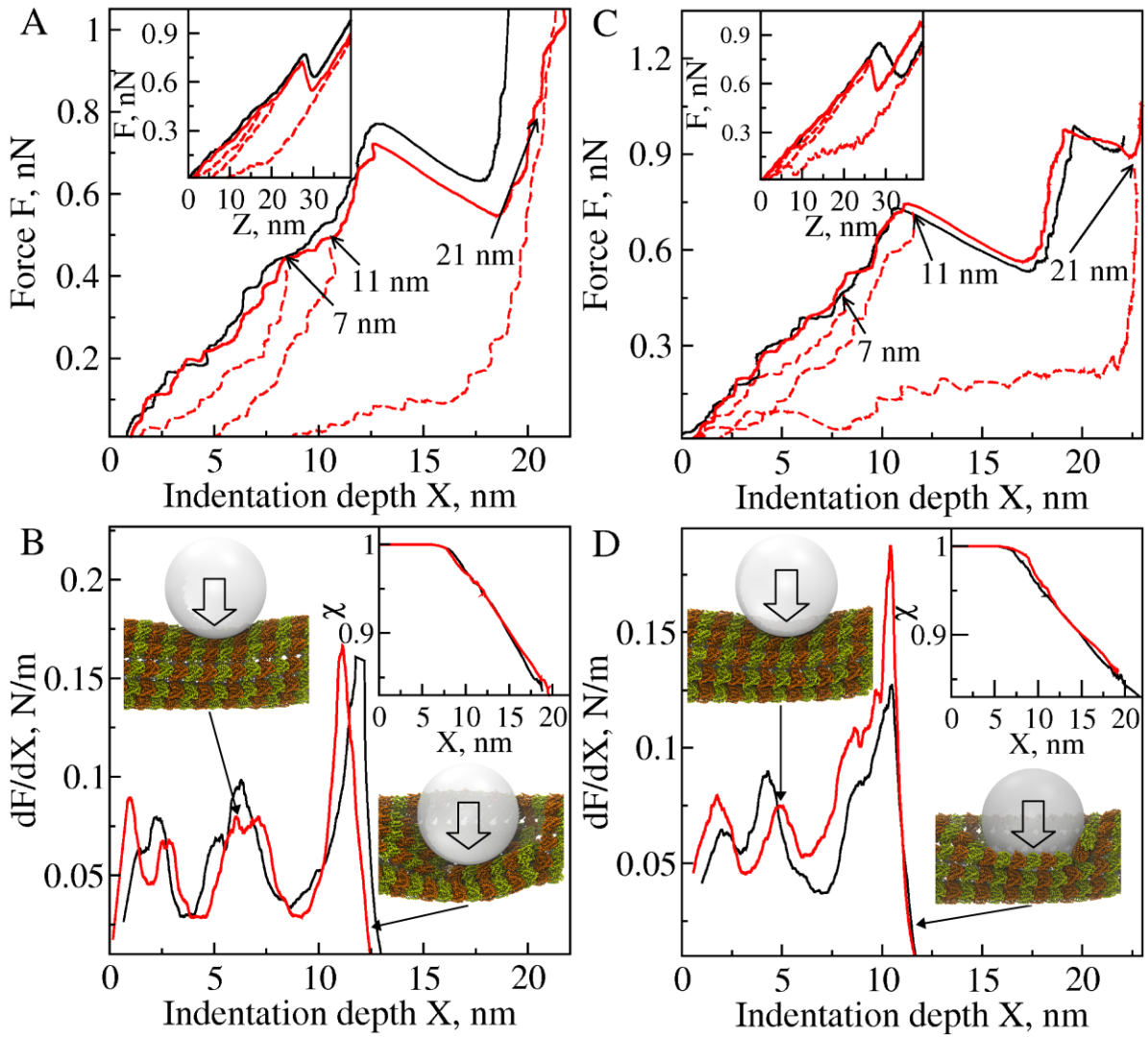

Fig. S2. Force spectra for indentation and retraction of the MT lattice *in silico* and corresponding structure alterations. Representative results for indentation points 3 (black) and 1 (red) in **A** and **B**, respectively, and for indentation points 5 (black) and 7 (red) in **C** and **D**, respectively, obtained with v_f = 1.0 μm/s and R_{tip} = 15 nm (see Fig. 3 for results obtained with smaller tip of R_{tip} = 10 nm). **A** and **C:** The *FX* curves (*FZ* curves are in the *inset*) for forward indentation (solid black and red curves). Curves for backward tip retraction (dashed red lines) were generated using the structures obtained from forward indentation for X = 7, 11, and 21 nm (indicated on the graphs). **B** and **D:** The slope of the *FX* curves *dF/dX* for the force spectra from panels **A** and **C**. Snapshots show the side-views of the MT structure before dissociation of the lateral bonds and after dissociation of the longitudinal bonds. *The insets* show the profiles of structure overlap χ vs. X, which demonstrate that the MT lattice in the fully collapsed state (X > 20 nm) is ~80-85% similar to the native state.

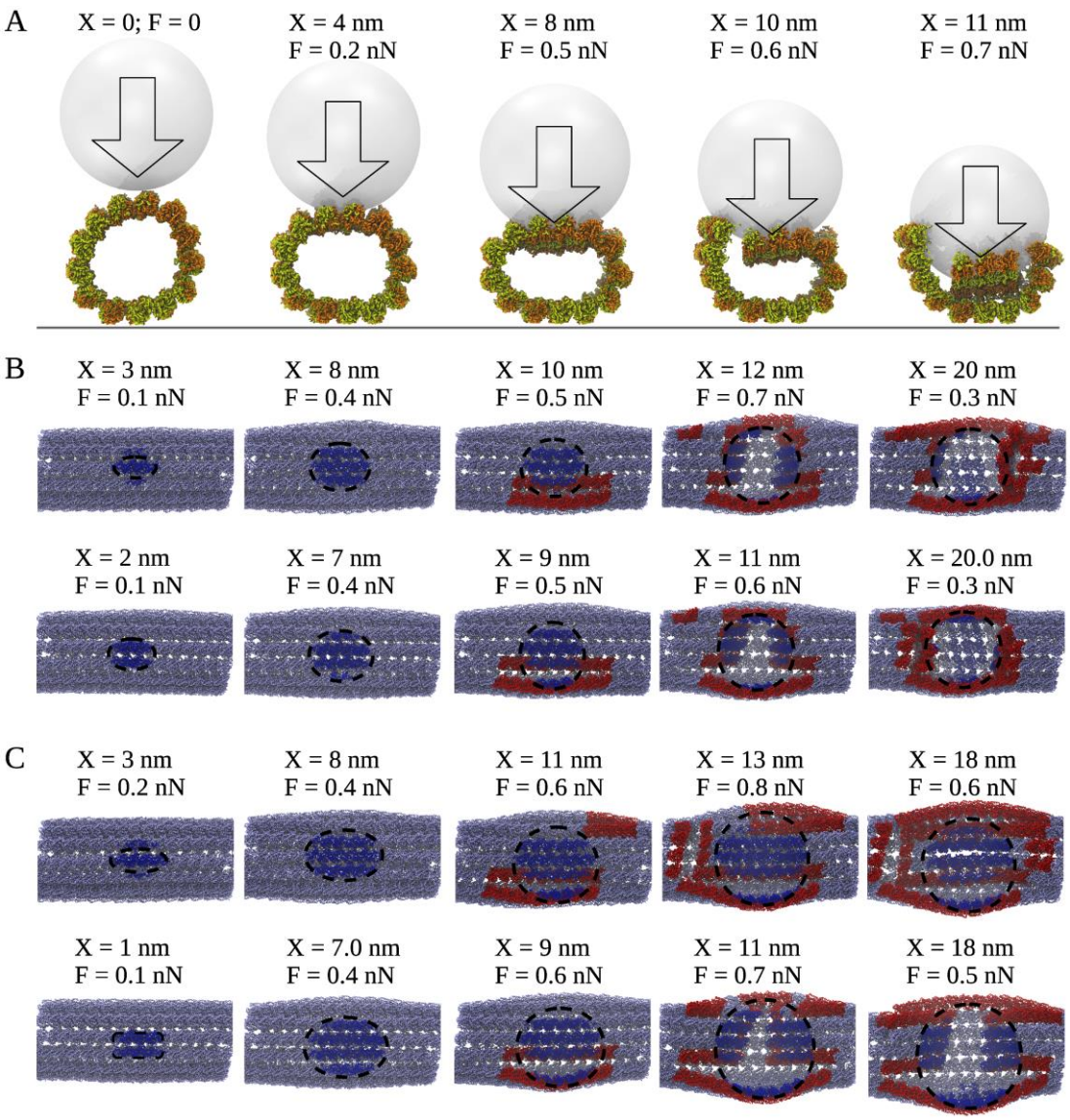

Fig. S3: Dynamic structure changes observed during mechanical compression of MT fragment MT8/13. **A:** Profiles of the MT lattice viewed along the MT cylinder axis for different extent of indentation obtained with R_{tip} = 15 nm (indentation point 7; see Fig. 1C). **B** and **C** show top views of the MT lattice for indentation points 3 (upper raw in **B**) and 6 (lower raw in **B**) obtained with smaller tip (R_{tip} = 10 nm), and for the indentation points 3 (upper raw in **C**) and 4 (lower raw in **C**) obtained with larger tip (R_{tip} = 15 nm). During compression, the MT structure (light blue) becomes deformed and there is an associated increase in the MT-tip contact area (encircled dark blue area). Subsequent increase in the compressive force results in the dissociation of lateral and longitudinal bonds (tubulin monomers with disrupted lateral and/or longitudinal interface(s) are shown in dark red).

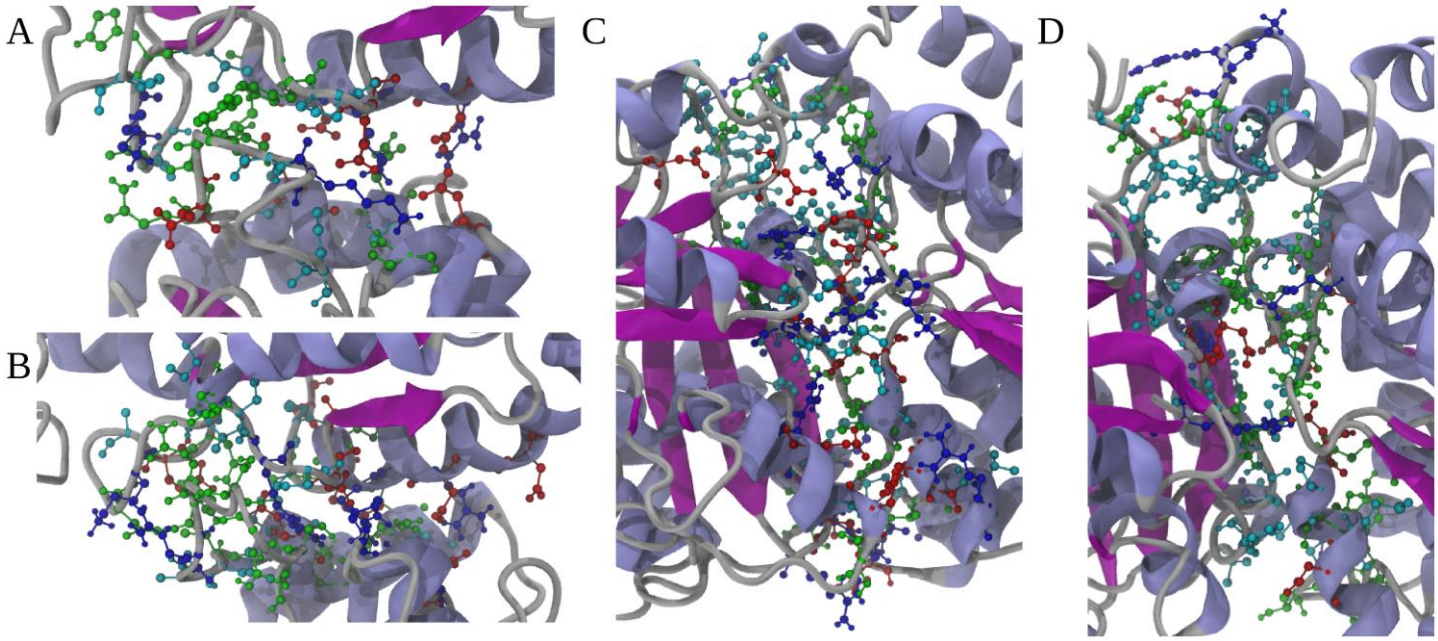

Fig. S4: Atomic representation of the interfaces, corresponding to lateral α-α (A) and β-β tubulin bonds (B), and the longitudinal intra-dimer (C) and inter-dimer bonds (D). The most stable side-chain contacts, i.e. the contacts that persist for 5 ns of simulations at equilibrium, are shown using the "balls-and-sticks" representation. The binary contact is defined as the contact between amino acids for which the distance between their C_α-atoms does not exceed 8 Å (see Materials and Methods). Color denotation: acidic side chains are in red, basic side-chains in blue, polar residues in green, and hydrophobic residues are in cyan. Color denotation for the secondary structure: α-helices (blue), β-sheets (red), and loops/turns (gray). The lateral interface between the α-tubulins contains ~19 side-chain contacts (**A**); the lateral interface between the β-tubulins contains ~21 contacts (**B**); the longitudinal intra-dimer interface is stabilized by ~78 contacts (**C**); and the longitudinal inter-dimer interface is stabilized by ~38 contacts (**D**).

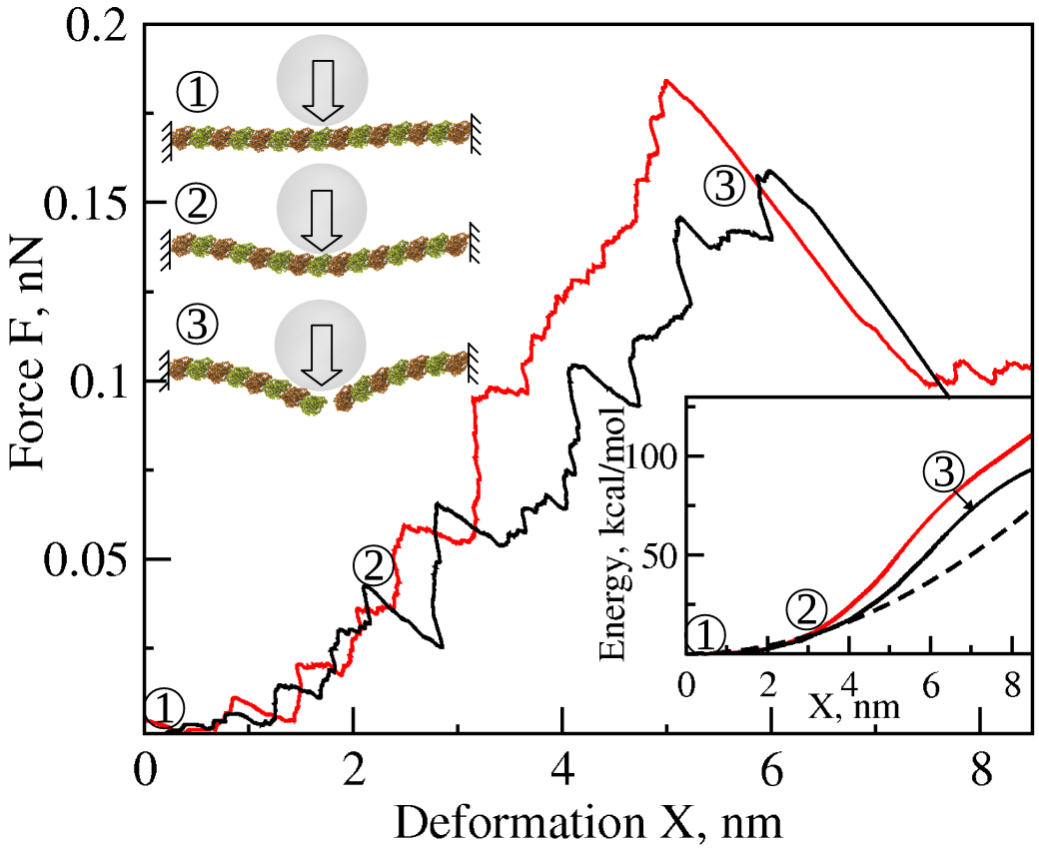

Fig. S5: Force-deformation spectra for single protofilament fragment of the MT cylinder. Shown are the typical examples of the force spectra for protofilament fragment PF8/1 (black and red solid curves) obtained by using the cantilever velocity v_f = 0.2 μm/s and spherical tip radius R_{tip} = 10 nm. Structures numbered 1-3, which show deformation progress, correspond to the black *FX* curve and represent the native state, the weakly bent state (X = 2 nm), and the strongly bent dissociated state (X = 6 nm), respectively. The tip shown with the vertical arrow deforms the protofilament until the dissociation of the longitudinal bond occurs. *The inset* shows the corresponding profiles of bending energy as a function of deformation for the estimation of the flexural rigidity. The dashed black curve is a fit of the quadratic function $V \sim X^2$ to the black curve of the energy V as a function of X, which shows the validity of the harmonic approximation used to calculate *EI* for protofilament fragments PF8/1, PF16/1, PF24/1, and PF32/1 (Table 3 in the main text).

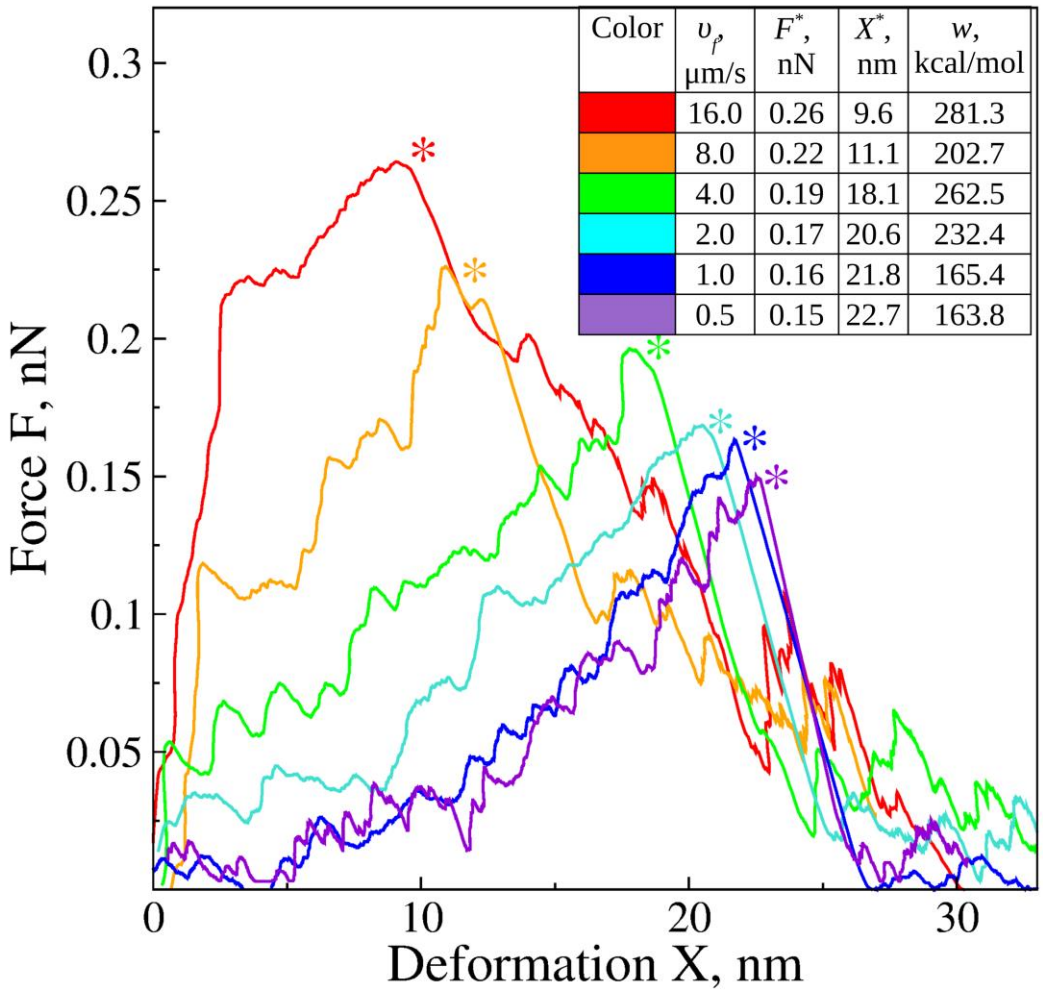

Fig. S6: Dependence of force-deformation spectra for single protofilament fragment on cantilever velocity. Shown in different colors for clarity are the typical examples of the force spectra (*FX* curves) for 24-dimer long protofilament fragment PF24/1 obtained by using the cantilever velocity v_f = 0.5 (violet), 1.0 (blue), 2.0 (turquoise), 4.0 (green), 8.0 (orange), and 16.0 μm/s (red color) and spherical tip (R_{tip} = 5 nm). The asterisks above the *FX* curves mark the onset of dissociation of the protofilament fragment, which occurs at the critical force F^* and critical deformation X^*. *The inset* is the summary of the values of F^*, X^*, and critical deformation work $w^* = \int_0^{X^*} F(X)dX$ (area under the *FX* curve up to $X = X^*$) obtained for different v_f. As v_f decreases, the *FX* curves change less and less. We also observe the convergence of F^*, X^*, and w^* with the decreasing velocity v_f , each approaching some stable values. This shows that *in silico* indentation experiments carried out at v_f = 0.5-1.0 μm/s cantilever velocity correspond to near-equilibrium conditions of the compressive force application.

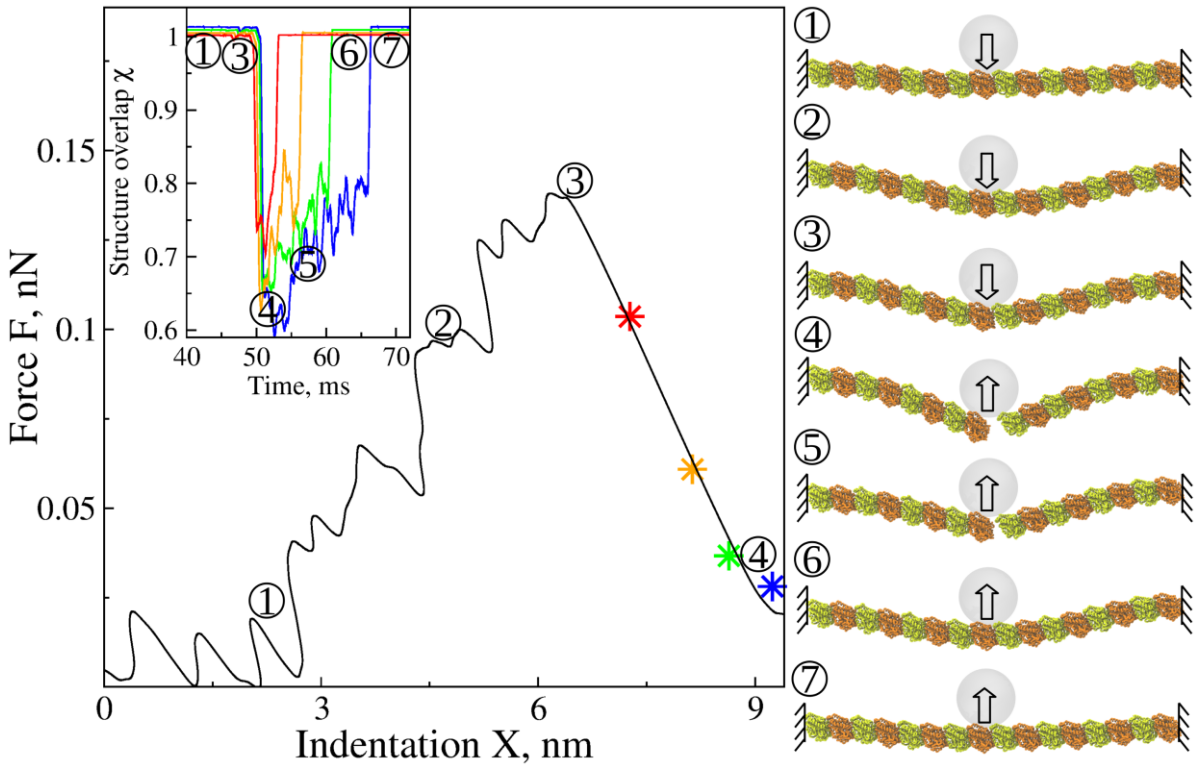

Fig. S7: Reversibility of longitudinal bonds' dissociation as observed for single protofilament fragment of the MT cylinder. Shown is the force-deformation spectrum for protofilament fragment PF8/1 (*FX* curve) obtained with v_f = 0.5 μm/s and R_{tip} = 5 nm. Structures numbered 1-4 which show deformation progress represent the near-native state (X = 2.0 nm; structure 1), weakly bent state (X = 4.5 nm; structure 2), strongly bent un-dissociated state (X = 6.5 nm; structure 3), and strongly bent dissociated state (X = 8.5 nm; structure 4), respectively. The tip (with vertical arrow) deforms the protofilament until the longitudinal bond dissociates. The asterisks mark the points for X = 7.0 nm (red), 8.0 nm (orange), 8.5 nm (green), and 9.2 nm deformations (blue), which correspond to the conformations of the strongly bent dissociated state of PF8/1. These 4 conformations were further used as initial structures in the simulations of force-quench retraction. *The inset* shows the time-profile of the structure overlap function χ (see Data analysis section) for the 4-th and 5-th dimer of PF8/1, which captures dissociation and subsequent re-formation of the longitudinal bond between the 4-th and 5-th dimer for all initial conditions used. Beyond the 50 ms time point, at which the bond dissociates (sharp drop in χ), the bond re-forms and the protofilament unbends over the 3, 6, 11, and 16 ms timeframe (χ approaches the unity) for all bond-dissociated structures corresponding to X = 7.0, 8.0, 8.5, and 9.2 nm deformations, respectively. Snapshots numbered 5-7, which correspond to X = 8.5 nm deformation (green asterisk), show the dynamics of bond re-formation and protofilament re-structuring observed in tip-retraction simulations. Hence, the longitudinal bond dissociation in short protofilament fragments (such as PF8/1) is reversible on the 10-20 ms timescale of our computational experiments.